C Journal of Carbon Research

MDPI

Article

Photocatalytic Materials Based on g-C_3N_4 Obtained by the One-Pot Calcination Method

Radik R. Shamilov [1,*], Zufar M. Muzipov [1], Dmitriy O. Sagdeev [1], Kirill V. Kholin [1], Alina F. Saifina [2], Aidar T. Gubaidullin [2] and Yuriy G. Galyametdinov [1,*]

[1] Department of Physical and Colloid Chemistry, Kazan National Research Technological University, 68 Karl Marx Str., 420015 Kazan, Russia
[2] Arbuzov Institute of Organic and Physical Chemistry, FRC Kazan Scientific Center of RAS, 8 Arbuzov Str., 420088 Kazan, Russia
* Correspondence: reedish@mail.ru (R.R.S.); yugal2002@mail.ru (Y.G.G.)

Abstract: Photocatalysts based on graphitic carbon nitride (g-C_3N_4) attracted considerable attention due to their efficiency in hydrogen production and decomposition of organic pollutants in aqueous solutions. In this work, a new approach to synthesis of g-C_3N_4-based heterostructures with improved photocatalytic properties was proposed. The properties of two different CdZnS/g-C_3N_4 and $ZnIn_2S_4$/g-C_3N_4 heterostructures synthesized and studied in the same conditions were compared. Pure g-C_3N_4 photocatalysts as well as CdZnS/g-C_3N_4 and $ZnIn_2S_4$/g-C_3N_4 heterostructures were synthesized using a one-pot method by calcining the mixture of the initial components. Photocatalytic properties of the synthesized substances were evaluated in a model reaction of rhodamine B decomposition induced by visible light. It was shown that ultrasonic treatment in the presence of a nonionic surfactant enhances the photocatalytic activity of g-C_3N_4 structures as a result of a higher photocatalyst dispersity. The electronic structures of the CdZnS/g-C_3N_4 and $ZnIn_2S_4$/g-C_3N_4 heterostructures were analyzed in detail. The photocatalytic activity of heterostructures was found to be 2–3-fold higher as compared with an unmodified g-C_3N_4 due to formation of a type II heterojunction and Z-scheme structures. Decomposition of rhodamine B occurred mostly via formation of active oxygen radicals by irradiation.

Keywords: photocatalysis; one-pot synthesis; g-C_3N_4; CdZnS; $ZnIn_2S_4$; heterostructures; decomposition of pollutants

Citation: Shamilov, R.R.; Muzipov, Z.M.; Sagdeev, D.O.; Kholin, K.V.; Saifina, A.F.; Gubaidullin, A.T.; Galyametdinov, Y.G. Photocatalytic Materials Based on g-C_3N_4 Obtained by the One-Pot Calcination Method. *C* **2023**, *9*, 85. https://doi.org/10.3390/c9030085

Academic Editor: Aleksey A. Vedyagin

Received: 25 July 2023
Revised: 28 August 2023
Accepted: 31 August 2023
Published: 2 September 2023

1. Introduction

Study and modification of photocatalytic properties of semiconductor nanostructured materials are among the most vibrant research trends in the last decade. Depending on the research problem, nanostructured photocatalysts can perform water splitting into hydrogen and oxygen, destruction of various organic pollutants, and reduce carbon dioxide to organic compounds induced by UV and visible light. Particular attention is paid to photocatalysts that absorb visible light and can be used in natural sunlight excitation conditions [1–4].

The presence of electron donors in water (and other compounds such as amines, alcohols, aldehydes, and carboxylic acids) intensifies formation of molecular hydrogen. In this regard, it is promising to use organic pollutants as electron donors, because they provide an opportunity for simultaneous hydrogen production and removal of organic pollutants contained in domestic and industrial wastewater [5,6].

There are various semiconductor materials used for photocatalytic reactions. Photocatalysts based on graphitic carbon nitride (g-C_3N_4) have great prospects for practical applications. They do not contain any toxic components and can be used both to produce hydrogen and decompose organic pollutants in water solutions. [7–10]. Recent studies demonstrated that the structures based on g-C_3N_4 are also effective in the reactions of decomposition of antimicrobial drugs and disinfection under the action of visible light [11].

They can exhibit multifunctional properties such as hydrazine sensing and hydrogen production [12]. They can be used in combination with photo-Fenton catalysts to remove persistent pollutants from water [13].

A number of simple methods can be applied to synthesis of g-C_3N_4 photocatalysts using available reagents such as urea, thiourea, melamine, and cyanuric acid. If synthesis according to these methods is preformed, an initial bulk structure of g-C_3N_4 is formed. It further splits into small layers by physical or chemical exfoliation, which enhances photocatalytic properties of the resulting compounds [7,14,15].

These compounds are capable of absorbing visible light. However, due to a charge recombination, their photocatalytic activity turns out to be low. In this regard, g-C_3N_4 materials are mostly used as components of heterostructures that also incorporate other compounds [8,9]. Among various types of heterojunctions, type II and Z-scheme compounds are the most important for increasing the photocatalytic efficiency [7–9].

Development of such hybrids with other semiconductors is an approach that contributes to separation of charge carriers into different phases and increases recombination lifetimes. It also favors redox interactions of these charges with surrounding molecules.

To create such heterojunctions, it is important to consider that the positions of the band gaps of C_3N_4 and another semiconductor should be shifted relative to each other. For effective absorption of visible light, it is necessary for the second semiconductor to have a band gap no greater than the respective value of C_3N_4 (about 2.7 eV).

There are many types of semiconductors that satisfy these requirements. Among them, photocatalysts based on cadmium sulfide nanostructures are interesting due to their catalytic properties exhibited under visible light, especially in hydrogen evolution reactions [16]. Synthesis of mixed CdZnS 'solid solution' semiconductors allows to control the bandgap of this material, and also considerably reduce surface photooxidation, which is a characteristic feature of CdS photocatalysts. Development of optimal synthesis methods is necessary for fabricating hybrid materials that are stable in photooxidation processes and possess good photocatalytic properties [17].

It was previously shown that synthesis of g-C_3N_4 hybrids with CdZnS semiconductors leads to a considerable increase in photocatalytic activity of the resulting materials in reactions of both hydrogen evolution from water and decomposition of organic compounds [18,19].

Depending on synthesis conditions, g-C_3N_4 и CdZnS can form hybrids with type II and Z-scheme heterojunctions [20]. Formation of Z-scheme heterojunctions results from a considerable shift of semiconductor bandgaps relative to each other. Such heterostructures can create electron-hole pairs with a high redox potential.

The work in [19] reports synthesis of CdZnS/g-C_3N_4 heterostructures using a simple one-pot method to calcine the mixture of precursors represented by thiourea and metal salts. The resulting materials possess good photocatalytic properties. This synthesis method is of undoubtful interest. For applied research, however, it is necessary to consider alternative methods that require smaller amounts of thiourea because its decomposition produces a large amount of toxic sulfur-containing byproducts [21].

Materials based on $ZnIn_2S_4$ can be considered as alternatives to cadmium-based catalysts. The bandgap of $ZnIn_2S_4$ (2.4 eV) is comparable to that of CdZnS (2.3–2.5 eV). This material also exhibits photocatalytic properties under visible light. The advantages of the $ZnIn_2S_4$ material are its high photostability and intrinsic nano- and microlayers that provide it with a high surface area [22,23].

Creation of g-C_3N_4 hybrid structures with $ZnIn_2S_4$ contributes to a more efficient charge separation and an additional increase in their photocatalytic activity. Previously, it was shown that $ZnIn_2S_4$/g-C_3N_4 heterostructures as well as CdZnS/g-C_3N_4 exhibit intensive photocatalytic properties in the reactions of water splitting and decomposition of organic compounds [24–26].

At the same time, g-C_3N_4 and $ZnIn_2S_4$ bandgaps have a little shift relative to each other. Therefore, $ZnIn_2S_4$/g-C_3N_4 hybrids are predominantly characterized by type I or type II heterojunctions.

A hydrothermal and solvothermal methods are the most commonly used approaches to synthesize $ZnIn_2S_4$ photocatalysts and their hybrid structures. During the synthesis process, $ZnIn_2S_4$ nanolayers are formed on the surface of a previously synthesized semiconductor particles (for example, g-C_3N_4). At high concentrations of initial components, formation of a separate $ZnIn_2S_4$ phase is also possible.

At the same time, there are no known one-pot methods of calcining the initial components for synthesis of $ZnIn_2S_4$/g-C_3N_4 heterostructures. Similar to CdZnS/g-C_3N_4, it can be assumed that formation of $ZnIn_2S_4$/g-C_3N_4 with effective photocatalytic properties as a result of high-temperature decomposition of thiourea.

In this work, we demonstrated an affordable one-pot method for synthesis of materials based on g-C_3N_4 and CdZnS/g-C_3N_4 and $ZnIn_2S_4$/g-C_3N_4 heterostructures. Decomposition of rhodamine B in water solutions was used as a sample reaction for photocatalytic studies to compare the properties of all the studied substances in the same conditions.

2. Materials and Methods

Materials: Melamine (99%, Vitareactiv, Russia), thiourea (99%, Sigma Aldrich, St. Louis, MO, USA), cadmium acetate (II) dihydrate (98%, Sigma Aldrich, St. Louis, MO, USA), zinc acetate (II) dihydrate (99%, Reahim, Russia), indium acetate (III) (99%, Sigma Aldrich, St. Louis, MO, USA), rhodamine B (99%, Lenreactiv, Russia), methylene blue (99%, Lenreactiv, Russia), neonol AF 9–12 (technical grade, Nizhnekamskneftekhim, Russia), 1,4-benzoquinone (99%, Reahim, Russia), ammonium oxalate monohydrate (99%, Lenreactiv, Russia), and isopropyl alcohol (99%, Vekton, Russia).

g-C_3N_4 structures were obtained by thermal decomposition of melamine at a heating rate of 5 °C/min to 550 °C (2 h) and 1-h exposure at 550 °C under argon atmosphere. In order to obtain CdZnS/g-C_3N_4 heterostructures, 0.266 g (1 mmol) of cadmium acetate dihydrate, 0.220 (1 mmol) of zinc acetate dihydrate, 0.381 g (5 mmol) of thiourea and 1 g (8 mmol) of melamine were mixed and finely ground in a mortar. The resulting composition was then calcined similarly to melamine. $ZnIn_2S_4$/g-C_3N_4 heterostructures were obtained by mixing 0.11 g (0.5 mmol) of zinc acetate dihydrate, 0.292 (1 mmol) of indium acetate, 0.381 g (5 mmol) of thiourea and 1 g (8 mmol) of melamine. Samples of CdZnS and $ZnIn_2S_4$ were synthesized in similar conditions without the use of melamine.

Elemental analysis of finely ground powders of the obtained samples was carried out on a Vario EL CUBE setup and using a Bruker M4 Tornado XRF analyzer.

The surfaces of the particles were characterized using a Carl Zeiss Evo scanning electron microscope. Sample images were obtained using a secondary electron detector. The samples were studied at the probe current I_{Probe} = 110 pA, at the accelerating voltage EHT = 6 kV.

Specific surface area studies were performed through the dye adsorption method. 40 mg of sample were dispersed in 200 mL of methylene blue solution (C = 0.02 g/L) vigorously stirred for 1 h to establish adsorption equilibrium. After that, the solution was left for 24 h in the dark for precipitation of the catalyst and then filtered through a 0.22 μm syringe filter. The concentration of the dye solution after achieving the equilibrium was determined by spectrophotometry at the 665 nm absorption maximum.

X-ray powder diffractograms were obtained on a Bruker D8 Advance diffractometer equipped with Vario attachment and Vantec linear PSD, using Cu radiation (40 kV, 40 mA) monochromated by the curved Johansson monochromator (λ Cu $K_{\alpha 1}$ 1.5406 Å). Room-temperature data were collected in the reflection mode with a flat-plate sample. The samples were loaded on a silicon plate, which reduces background scattering. Patterns were recorded in the 2θ range between 3° and 95°, in 0.008° steps, with a step time of 1–5 s. Processing of the obtained data was performed using EVA software package [27]. Full-profile analysis of diffraction data by the Rietveld method and estimation of the

dimensional characteristics of nanoparticles crystallites were performed using the TOPAS software package [28].

ICDD PDF-2 Release 2005 powder diffraction database was used for the identification of crystalline modifications.

UV-Vis absorption spectra were recorded by Perkin Elmer LAMBDA 35 spectrophotometer. Luminescence spectra were collected on Varian Cary Eclipse spectrofluorimeter. FTIR spectra were obtained on a Bruker ALPHA-T S/N 102706 Fourier spectrometer. Hydrodynamic size of nanoparticles was measured by dynamic light scattering method at Malvern Zetasizer Nano-ZS setup.

Relative quantum yields of the samples were calculated with the relation to the reference system that was the solution of quinine sulfate in 0.1 M H_2SO_4 (QY = 0.54) at the excitation wavelength of 350 nm. The intensity of absorption in the form of an aqueous dispersion at a given wavelength did not exceed 0.05 a.u.

For photocatalytic studies, 5 mg (typically) of each sample were preliminarily sonicated in 15 mL of distilled water for 10 min (44 kHz, 100 W). The solution of rhodamine B (0.8 mL, 0.001 mol/L) was then added to the mixture and stirred in the dark for 30 min to reach adsorption equilibrium (T = 25 °C).

Photocatalytic studies were carried out by decomposition of rhodamine B (RhB) using a 50 W LED chip (COB module) with an emission peak of 452 nm as a radiation source (FWHM = 26 nm). The photodecomposition was controlled by sampling at certain time intervals. The temperature of the reaction mixture was maintained within 25 ± 0.3 °C. The samples were centrifuged at 3000 rpm for 15 min to precipitate the photocatalyst suspension.

3. Results and Discussion

3.1. One-Pot Synthesis of g-C_3N_4 Structures

Synthesis of g-C_3N_4 structures was carried out by decomposition of melamine at the temperature of 550 °C. CdZnS/g-C_3N_4 and $ZnIn_2S_4$/g-C_3N_4 heterostructures were synthesized from melamine and the mixture of acetates of these metals in excess of thiourea as a source of sulfur (Figure 1).

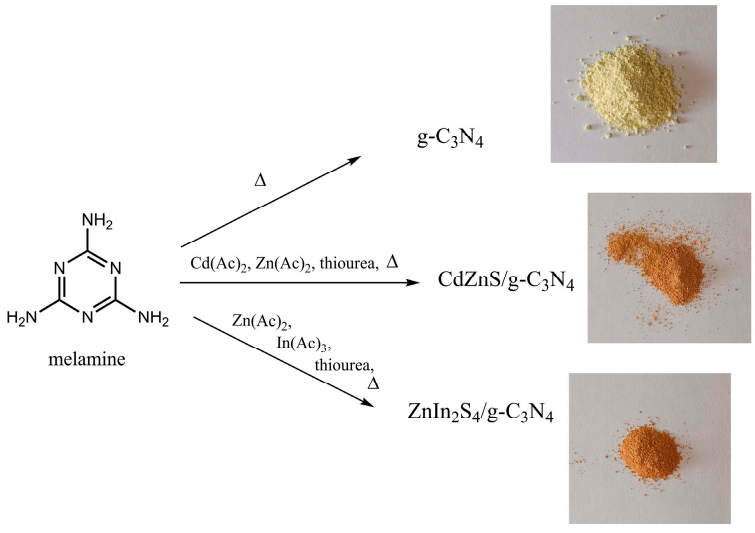

Figure 1. Synthesis scheme and photos of the studied materials.

Previously, a one-stage strategy was demonstrated for synthesis CdZnS/g-C_3N_4 heterostructures from thiourea [19]. Thiourea decomposes at high temperatures by forming g-C_3N_4 and releasing considerable amounts of volatile products, including toxic sulfur-containing compounds. In our work, melamine was the main component used for synthesis of g-C_3N_4 structures, while thiourea was used as a source of sulfur for synthesis of CdZnS

and $ZnIn_2S_4$. Based on the previous studies [18,19], we selected the optimal mass ratio of the initial components (approximately 3:1 of g-C_3N_4 and CdZnS or $ZnIn_2S_4$, respectively) for synthesis of the heterostructures.

3.2. Composition and Structure Characteristics

Formation of C_3N_4 structures was confirmed by elemental analysis (Table 1). An excess amount of nitrogen and hydrogen in the studied components indicates the presence of residual amine groups of melamine. A small amount of oxygen in the samples is due to the presence of adsorbed water and oxygen molecules, which take part in the photocatalytic process.

Table 1. Data of elemental analysis of the studied samples (weight ratio).

Sample	Vario El Cube					M4 Tornado		
	C, %	H, %	N, %	S, %	O, %	Zn, %	Cd, %	In, %
g-C_3N_4	34.31	0.69	61.72		3.28			
CdZnS/g-C_3N_4	27.83	0.59	50.11	6.22	2.48	6.74	6.03	
$ZnIn_2S_4$/g-C_3N_4	25.15	0.52	45.41	8.66	2.20	7.78		10.28

The molar ratio of metals in heterostructures differs from their amount in the initial precursors, which is probably due to determination of the elemental composition by X-ray fluorescence analysis. It can be reliably stated that the mass fraction of the g-C_3N_4 phase in the CdZnS/g-C_3N_4 and $ZnIn_2S_4$/g-C_3N_4 heterostructures is more than 70%, which also indicates that its molar fraction is predominant.

The morphology of the samples was investigated by scanning electron microscopy (SEM) (Figure 2). At low magnification, formation of a lamellar g-C_3N_4 structure can be distinctly observed. The CdZnS/g-C_3N_4 and $ZnIn_2S_4$/g-C_3N_4 samples possess a more porous structure. Pores in the heterostructures emerge because of abundant volatile products that release during decomposition of thiourea and the salts of the respective metals. Absence of g-C_3N_4 sheets indicates a good mutual distribution of the two phases. At higher magnification, the g-C_3N_4 sample exhibits formation of large aggregates. In CdZnS/g-C_3N_4 and $ZnIn_2S_4$/g-C_3N_4 samples, the structure is represented by aggregates of smaller particles.

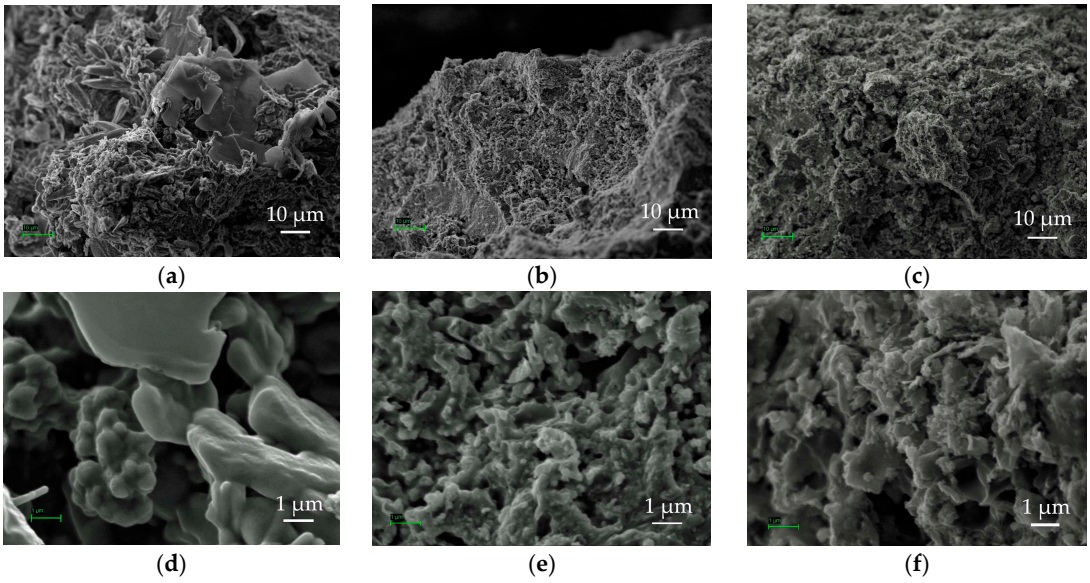

Figure 2. SEM images of the samples obtained at ×1000 (**a**–**c**) and ×10,000 (**d**–**f**) magnification: (**a**,**d**) g-C_3N_4; (**b**,**e**) CdZnS/g-C_3N_4; (**c**,**f**) $ZnIn_2S_4$/g-C_3N_4.

3.3. Specific Surface Area Measurements

The photocatalytic activity of materials depends significantly on their specific surface area (SSA). An increase in the photocatalytic efficiency of heterostructures can be associated not only with a more efficient charge separation, but also with an increase in the specific surface area of the materials.

The SSA values of the samples were determined by the methylene blue (MB) adsorption method described in [29] as follows:

$$SSA = N_A \cdot S_{MB} \cdot (C_0 - C_E) \cdot V / M_{MB} \cdot m_s \quad (1)$$

where N_A is the Avogadro constant ($6.02 \cdot 10^{23}$ mol^{-1}), S_{MB} is the surface coverage per molecule of MB (~1.35 nm^2), C_0 and C_E are the initial and equilibrium concentrations of MB, V is the volume of the MB solution, M_{MB} is the molecular mass of MB, and m_s is the weight of the sample, respectively.

The specific surface areas of the g-C_3N_4, CdZnS/g-C_3N_4 and $ZnIn_2S_4$/g-C_3N_4 compounds were found to be 15.3, 12.3 and 15.1 m^2/g, respectively. The values obtained for all the samples are approximately equal, which is probably due to similar conditions of their synthesis. Low specific surface area values can be explained by the high-temperature synthesis method, which results in a denser fusion of different phases and a decrease in the porosity of the material.

3.4. XRD Studies

The samples of g-C_3N_4, CdZnS/g-C_3N_4, and $ZnIn_2S_4$/g-C_3N_4 were analyzed by X-ray powder diffraction method. The experimental diffraction pattern for pure g-C_3N_4 (Figure 3a, black curve) shows interference peaks that are characteristic of the ordered structure of g-C_3N_4 [7,30]. According to the literature data for the structure of graphitic carbon nitride, a peak with an angular position of $2\theta \sim 27.5^0$ corresponds to diffraction from crystallographic planes (002) and is determined by the ordering formed due to $\pi \ldots \pi$ stacking of trisubstituted heptazine fragments, while a less intense peak at $2\theta \sim 12.9^\circ$ (plane 100) characterizes the ordering of molecular structures in planes of these fragments.

Considering the heterostructure of the CdZnS/g-C_3N_4 type, the structure of the initial carbon nitride retains, and both peaks that are characteristic of carbon nitride are observed on the experimental curve (Figure 3a, blue curve). Additional peaks observed in the diffraction pattern were analyzed using the powder database and identified as the ones representing the polycrystalline form of Zinc Cadmium Sulfide, $Zn_{0.5}Cd_{0.5}S$ (ref. No. 01-089-2943) (Figure 3b). In general, the observed broadening of the diffraction peaks on all the experimental curves indicates a favored formation of nanostructured materials with very small sizes of crystallites.

In the X-ray diffraction pattern of the $ZnIn_2S_4$/g-C_3N_4 heterostructure, the first peak (100) is absent (Figure 3a, red curve). This may apparently indicate a substantial deterioration in ordering. At the same time, a comparative search in the PDF-2 database for other diffraction peaks on the experimental curve indicates not only the presence of a polycrystalline form of Indium Zinc Sulfide, In_2ZnS_4 (Ref.No. 03-065-2023) in this sample (Figure 3c), but also a possible formation and presence of Zinc Indium Sulfide, $Zn_3(In_2S_6)$ (Ref.No. 01-080-0835) (Figure 3d).

For all the studied samples, we calculated the average sizes of both graphitic carbon nitride crystallites and other crystalline phases using the positions and shapes of the most intense diffraction peaks. All data are summarized in Table S1. A full-profile analysis of the diffraction curves indicated that the average sizes of crystallites of all the crystalline phases in the samples did not exceed several nanometers. For the g-C_3N_4 phase crystallites, the crystallite sizes was found to be in the range of 1–10 nm and the crystallites themselves were noticeably anisometric. The sizes of crystallites in the $ZnIn_2S_4$/g-C_3N_4 phase were in the range of 4–11 nm, and the sizes of crystallites of CdZnS/g-C_3N_4 phase distributed

in the range of 4.5–15.9 nm. The crystallites of both these phases were elongated in one direction.

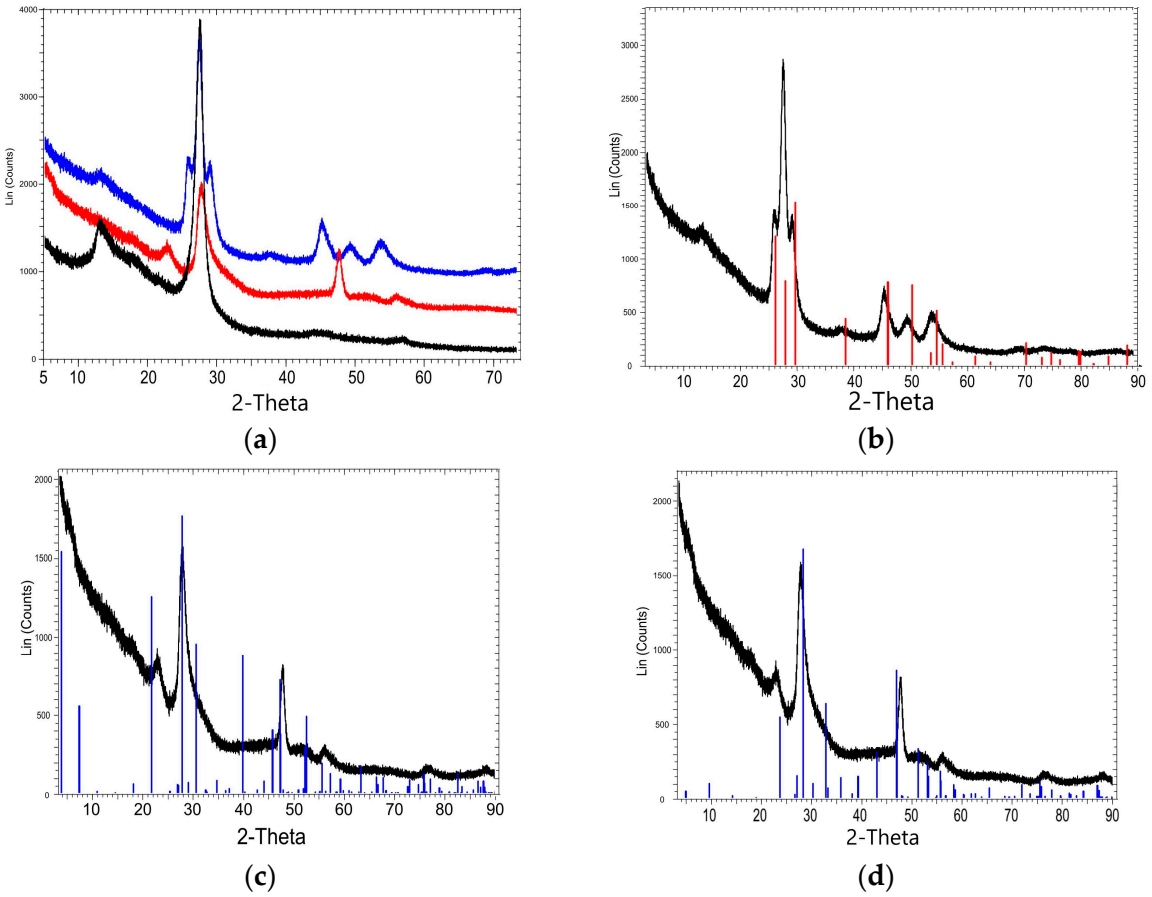

Figure 3. Experimental PXRD powder diffraction patterns: (**a**) the g-C_3N_4 (black curve), CdZnS/g-C_3N_4 (blue curve) and $ZnIn_2S_4$/g-C_3N_4 (red curve) samples. The curves were shifted relative to each other along the intensity axis for visual clarity; (**b**) the heterostructure of CdZnS/g-C_3N_4 type, the interference peaks corresponding to the crystalline form of $Zn_{0.5}Cd_{0.5}S$ (Ref.No. 01-089-2943) are shown by red vertical dashes; (**c**,**d**) the heterostructure of $ZnIn_2S_4$/g-C_3N_4 type, the interference peaks corresponding to the crystalline form of In_2ZnS_4 (Ref.No. 03-065-2023) (**c**) and $Zn_3(In_2S_6)$ (Ref.No. 01-080-0835) (**d**) are shown by blue vertical dashes.

3.5. FTIR and Optical Characteristics

On the FTIR spectra, all the samples exhibit absorption peaks that are characteristic of the g-C_3N_4 structures (Figure 4). The broad band at 3000–3300 cm^{-1} can be attributed to stretching vibrations of the N–H bond and residual surface amine and hydroxyl groups. Intense bands in the range of 1200–1650 cm^{-1} can be attributed to the C–N bonds of the heterocyclic ring. A narrow peak at 808 cm^{-1} corresponds to bending vibrations of triazine units. Similar absorption bands in the FTIR spectra of the CdZnS/g-C_3N_4 and $ZnIn_2S_4$/g-C_3N_4 heterostructures indicate the presence of a well-formed g-C_3N_4 phase in these samples.

All the samples can absorb light in broad UV and visible ranges (Figure 5a). However, CdZnS/g-C_3N_4 and $ZnIn_2S_4$/g-C_3N_4 heterostructures demonstrate a more intensive absorbance in the visible region as compared with g-C_3N_4. The bandgap energy of direct transitions was calculated for the g-C_3N_4 structure by the Kubelka–Munk method from the Tauc plots and was found to be 2.76 eV. This value is consistent with the previous data [19]. The CdZnS/g-C_3N_4 and $ZnIn_2S_4$/g-C_3N_4 samples showed the decrease in the bandgap energy to 2.59 and 2.62 eV, respectively (direct transitions) as the result of forming hybrid

structures. The synthesized compounds are, therefore, capable of absorbing light more efficiently in the visible region of the spectrum. The band gaps of the individual CdZnS and $ZnIn_2S_4$ components were 2.43 and 2.51 eV, respectively, which agrees with the previous data [19,24].

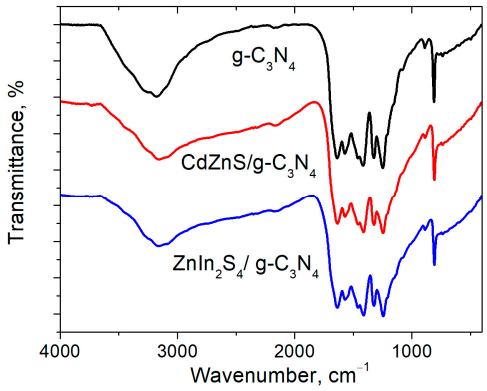

Figure 4. FTIR spectra of the samples.

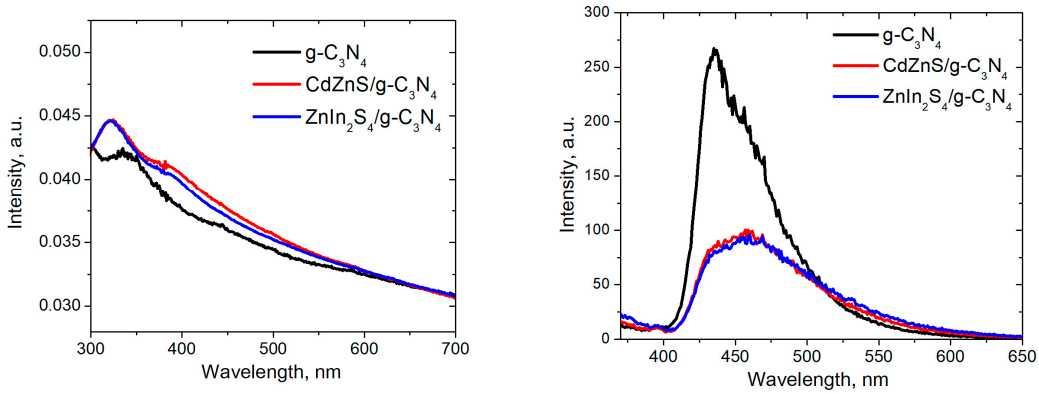

Figure 5. (**a**) Light absorbance; (**b**) luminescence spectra of the samples.

The study of the luminescence spectra provided additional information on the efficiency of charge carrier separation in the synthesized semiconductor materials. The resulting structures exhibit a low-intensity luminescence. The g-C_3N_4 sample has a broad luminescence band with the maximum at 435 nm, the relative quantum yield was calculated to be 4.2% (Figure 5b). In the heterostructures, the luminescence intensity is considerably reduced and the emission peak is shifted to the red region, while the relative quantum yield for CdZnS/g-C_3N_4 and $ZnIn_2S_4$/g-C_3N_4 samples was 2.2 and 1.8%, respectively. A decrease in the luminescence intensity can be explained by an increase in lifetimes of photoexcited states of charge carriers [20,24]. The resulting more efficient spatial separation in heterostructures favors interactions with surrounding molecules [19,24,25].

3.6. Effect of Surfactants on the Photocatalytic Properties of g-C_3N_4

The obtained materials possess the properties of heterogeneous catalysts and their photocatalytic properties are highly dependent on the specific surface area. The simplest and the most common method of splitting of these structures into small layers (exfoliation) of graphitic C_3N_4 is an ultrasonic treatment. Various surfactants can be used to improve their dispersity. Previously, it was shown that addition of anionic or cationic surfactants to the media can improve photocatalytic properties of heterostructures based on g-C_3N_4 [31]. It was reported that a positive effect is in this case provided by improved separation of

charge carriers on the surfaces of the particles and preventing them from agglomeration during synthesis.

The effect of nonionic surfactants on the photocatalytic properties of materials based on g-C_3N_4 has not been adequately studied. As it was previously shown in our studies, ultrasonic treatment of dispersions of carbon nanostructures in the presence of a nonionic surfactant based on ethoxylated isononylphenol can lead to a significant increase in their stability and dispersity. The best effect is provided by surfactants with the oxyethylation degree n = 8–12 [32,33].

In this work, we studied the effect of ultrasonic treatment of g-C_3N_4 structures in water in the presence of nonionic ethoxylated isononylphenol with the degree of oxyethylation n = 12 (neonol AF 9-12) on their degree of dispersion and photocatalytic properties.

It was found that the highest colloidal stability of the g-C_3N_4 dispersion in water within an hour after ultrasonic treatment is achieved with the surfactant concentration of 0.01% (Figure 6a). According to the dynamic light scattering data, ultrasonic treatment in the presence of surfactants increased dispersity of the samples (Figure 6b).

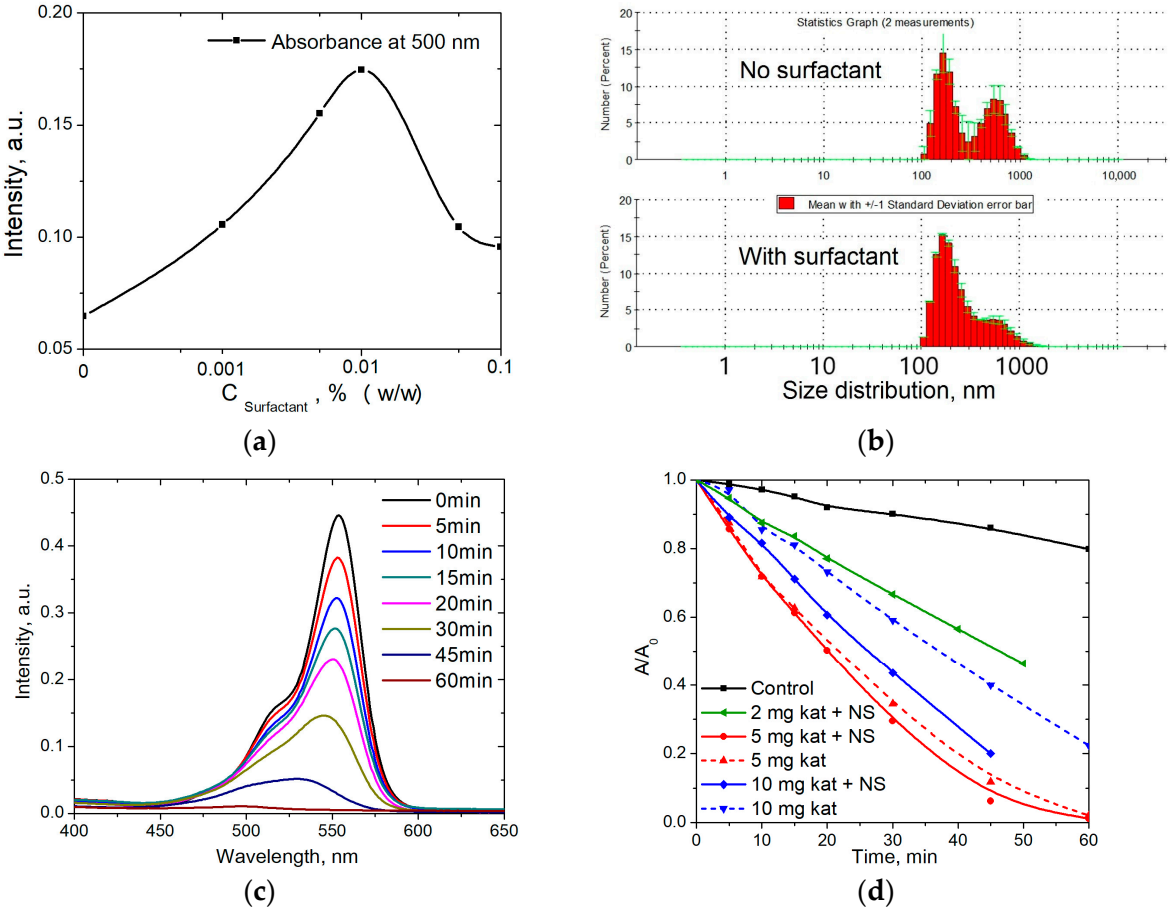

Figure 6. (**a**) Light absorption intensity of g-C_3N_4 dispersions vs. surfactant concentration; (**b**) g-C_3N_4 hydrodynamic size distribution histogram; (**c**) absorption spectra of the reaction mixture vs. irradiation time; (**d**) kinetic curves of RhB destruction depending on the g-C_3N_4 concentration and the presence of nonionic surfactant (NS).

The photocatalytic properties of the synthesized structures were studied using the model reaction of rhodamine B (RhB) decomposition. The dye decomposition rate was monitored by the intensity of the RhB absorption peak at 554 nm (Figure 6c). Based on

these data, the kinetic curves of the decomposition reaction were plotted and the reaction rate constants were calculated according to the first order reaction rate law:

$$\ln(A/A_0) = -kt. \quad (2)$$

where A is the intensity of the RhB absorption peak at t time, A_0 is the intensity of RhB peak at the beginning of reaction.

The efficiency of photocatalytic decomposition of organic compounds is highly dependent on the intensity of light absorbed by a sample, which is determined by the concentration of a catalyst and reagents, the design of a reactor, and other parameters. We initially selected the optimal concentration of RhB for our studies and also determined the effective concentration of the photocatalyst in the reaction mixture.

The decomposition rate of RhB under irradiation without a catalyst was shown to be quite low (Figure 6d). When 2 mg of the catalyst were added to the reaction mixture (0.013% of the total weight of the solution), we observed a noticeable increase in the dye decomposition reaction rate. The maximum increase in the photodecomposition rate was observed for 5 mg (0.033%) of g-C_3N_4. An increase in the catalyst concentration to 10 mg (0.067%) led to a decrease in the decomposition rate that was probably due to an intensive aggregation of g-C_3N_4 particles.

Dispersion with a nonionic surfactant demonstrated an additional enhancement of the photocatalytic properties of g-C_3N_4 (Figure 6d). In this case, the influence of surfactants is more pronounced at higher concentrations of the catalyst in the reaction mixture. It was determined that the dispersion of 5 mg of the catalyst in the presence of surfactants provided the 12% increase in the reaction rate constant. With 10 mg of g-C_3N_4, the increase in the reaction rate constant was 54%. Nevertheless, the maximum efficiency of photocatalysis was observed with 5 mg of the added catalyst. This amount of the catalyst was, therefore, used in our further experiments.

3.7. Study of the Photocatalytic Activity of Heterostructures

The photocatalytic activity of the pure g-C_3N_4 structures is quite low, which can be explained by the presence of a large number of charge carrier recombination centers on their surfaces, where the photoexcitation energy may be lost. Therefore, it is necessary to spatially separate the excited electrons and holes. A possible solution is to create hybrid heterostructures with other materials.

At the next step of this work, we studied the photocatalytic properties of heterostructures based on g-C_3N_4 with a low content of the CdZnS and $ZnIn_2S_4$ semiconductor materials synthesized using a simple one-pot method.

The charge carrier separation efficiency was evaluated for these heterostructures from the energy diagram, which was plotted using the values of the band gap calculated for the individual components (Figure 7).

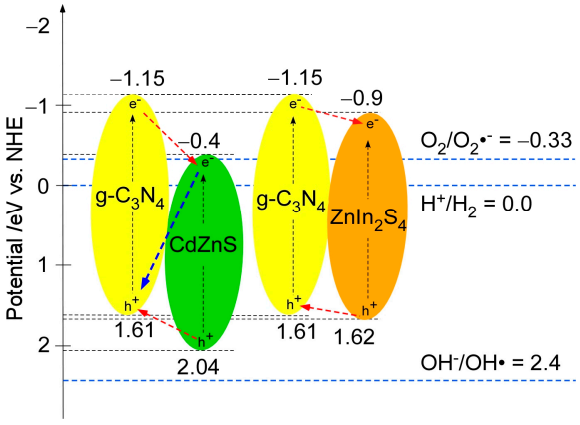

Figure 7. Bandgap structure diagram of CdZnS/g-C_3N_4 and $ZnIn_2S_4$/g-C_3N_4.

The band edge positions of the valence and conduction bands of semiconductors can be calculated as follows [34]:

$$E_{VB} = X - E_e + 0.5E_g, \quad (3)$$

$$E_{CB} = E_{VB} - E_g, \quad (4)$$

where X is the absolute electronegativity of the semiconductor, E_e is the energy of free electrons on the hydrogen scale (4.5 eV), and E_g is the band gap energy of the semiconductor.

The X values for g-C_3N_4, CdZnS, and $ZnIn_2S_4$ were found to be 4.73, 5.32, and 4.86 eV, respectively [25,35]. The calculated values of E_{CB} and E_{VB} of the components are consistent with the data of the previous studies.

According to the diagram, the energy levels of individual semiconductors are shifted relative to each other, which allows to form heterojunction type II (Figure 7, red arrows) or Z-scheme (Figure 7, blue arrow).

Compounds with such bandgap properties can be used both for hydrogen production and photooxidation of organic compounds. However, the electropositivity of the photogenerated holes in both heterostructures is not sufficient for generating nonspecific OH· radicals directly from water (Figure 7, blue dashed line). Therefore, oxidation is expected to predominantly occur via formation of $O_2\cdot^-$ radicals.

Experimental results show that the photocatalytic properties of heterostructures are significantly better than those of pure g-C_3N_4 (Figure 8a). According to the calculated values, the RhB decomposition rate constant in the presence of $ZnIn_2S_4$/g-C_3N_4 and CdZnS/g-C_3N_4 was almost 2- and 3-fold higher, respectively, than the rate constant in presence of pure g-C_3N_4 (Figure 8b).

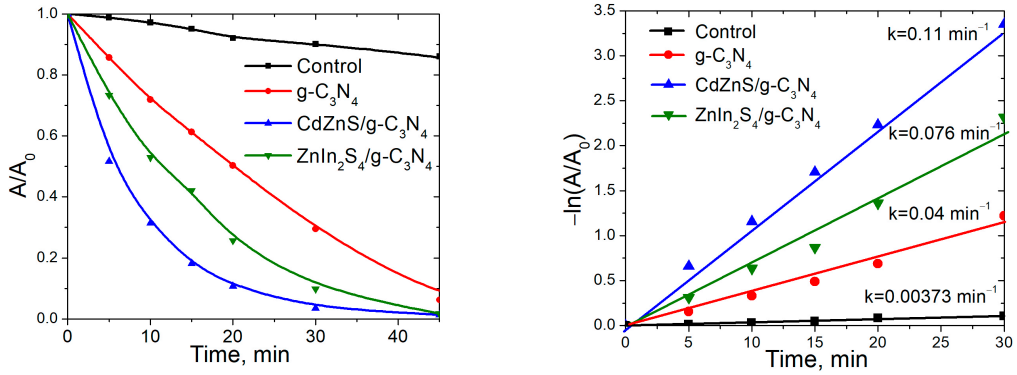

Figure 8. (**a**) RhB decomposition kinetic curves for different catalysts; (**b**) kinetics fit of RhB degradation in solutions based on equation 2.

A significant increase in the photocatalytic efficiency of heterostructures confirms formation of a heterojunction between two types of the semiconductor. According to the diagram, we assume formation of a heterojunction with the type-II electron migration in $ZnIn_2S_4$/g-C_3N_4 heterostructures (Figure 7, red arrows). As a result of the transfer of charge carriers from one material to another in the heterostructures, the lifetime of the excited state of electrons and holes increases so as the probability of their transfer to the surface of the photocatalyst and interaction with surrounding molecules.

In the CdZnS/g-C_3N_4 heterostructures, the levels of the individual components are more substantially shifted from each other as compared with the $ZnIn_2S_4$/g-C_3N_4 sample. Therefore, two pathways of charge separation are possible. The first one is a type II transition of the charge carriers from one material to another that provides their free energy reduction (Figure 7, red arrows). Another possible option is recombination of photoexcited electrons from a low-energy CdZnS with the g-C_3N_4 holes (Figure 7, blue arrow). In this

case, charge carriers with higher redox properties are involved in the photocatalytic process (Z-scheme).

The studied heterostructures have similar specific surface areas and their difference in photocatalytic properties is not related to surface effects. Close quantum yields of the samples also indicate similar separation efficiencies of their charge carriers.

Higher photocatalytic activities of the CdZnS/g-C_3N_4 samples may also be indicative of a Z-scheme heterojunction in such heterostructures. This suggestion is consistent with the results of the work reporting a similar synthesis approach to CdZnS/g-C_3N_4 heterostructures [19]. A Type II charge separation would lead to formation of photogenerated electrons and holes with a lower redox potential as compared to the $ZnIn_2S_4$/g-C_3N_4 sample.

Since the conductive level of CdZnS (−0.4 eV) in our samples is more negative than the level required for formation of $O_2\cdot^-$ radical anions (−0.33 eV), radical trapping experiments cannot give a distinct prediction about a possibility of these processes. Therefore, we consider that both types of such a heterojunction are possible in the studied CdZnS/g-C_3N_4 heterostructures.

The respective characterization of the studied samples is summarized in Table 2.

Table 2. The main characteristics of the studied samples.

Sample	Specific Surface Area, m^2/g	Bandgap, eV	Quantum Yield, %	RhB Decomposition Rate Constant, min^{-1}
g-C_3N_4	15.3	2.76	4.2	0.04
CdZnS/g-C_3N_4	12.3	2.59	2.2	0.11
$ZnIn_2S_4$/g-C_3N_4	15.1	2.62	1.8	0.076

3.8. RhB Photocatalytic Degradation Mechanism

Interactions of photogenerated electrones and holes on the photocatalyst surface with the solvent (water) molecules lead to formation of highly active species capable of reacting with dye molecules in the reaction media [7,9,36,37]. Oxygen molecules adsorbed on the catalyst surface favor formation of $O_2\cdot^-$ radical anions, which are also involved in oxidation of organic compounds:

$$e^- + O_2 \rightarrow O_2\cdot^-, \quad (5)$$

$$O_2\cdot^- + 2H^+ + 2\,e^- \rightarrow H_2O_2, \quad (6)$$

$$H_2O_2 + e^- \rightarrow OH^- + OH\cdot, \quad (7)$$

$$\text{dye} + OH\cdot\ (h^+ \text{ or } O_2\cdot^-) \rightarrow \text{decomposition products}. \quad (8)$$

The mechanism of the RhB photodecomposition reactions was studied in radical trapping experiments. Benzoquinone, ammonium oxalate and isopropyl alcohol were used as scavengers for $O_2\cdot^-$, h^+, and OH· active species [38]. The values of the rate constants of these reactions are represented in the diagram (Figure 9).

The results show a substantially slower degradation of RhB in the presence of benzoquinone, which indicates a direct participation of $O_2\cdot^-$ species in oxidation reactions. The decrease in the reaction rate constant was found to be 87% for CdZnS/g-C_3N_4 and 88% for $ZnIn_2S_4$/g-C_3N_4.

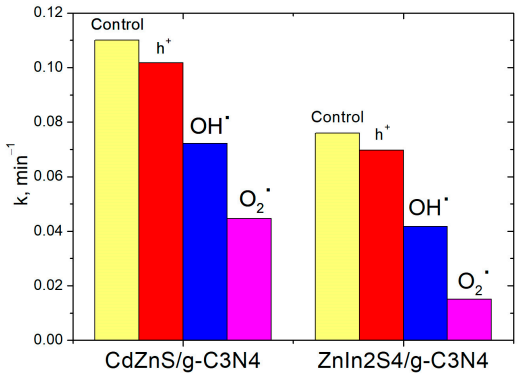

Figure 9. RhB decomposition rate constants in the presence of active species scavengers.

The reaction with ammonium oxalate as a hole acceptor does not lead to a significant change in the dye decomposition rate, which may indicate that decomposition of RhB by the holes is insignificant.

In the presence of isopropyl alcohol, the rate constant of RhB decomposition decreased moderately for both types of heterostructures, which indicates participation of OH· radicals in dye oxidation. According to the diagram (Figure 7), the holes do not possess a sufficient positive potential to generate OH· radicals from water. Therefore, it can be assumed that OH· radicals are formed from adsorbed oxygen molecules in a series of reactions summarized in Equations (4)–(6).

Thus, we can conclude that the photocatalytic decomposition of RhB molecules in the presence of synthesized heterostructures occurs mainly through interactions of photoexcited electrons with surface oxygen molecules and formation of $O_2 \cdot^-$ radicals. In general, the contribution of active species to the dye oxidation process can be described as follows: $O_2 \cdot^- > OH \cdot > h^+$.

4. Conclusions

Structural and photocatalytic properties of g-C_3N_4 materials, CdZnS/g-C_3N_4 and $ZnIn_2S_4$/g-C_3N_4 heterostructures obtained by a simple one-pot method were studied. Ultrasonic treatment in the presence of nonionic surfactants was shown to enhance photocatalytic properties of g-C_3N_4 structures as a result of their higher dispersity. Incorporation of two different semiconductor materials into heterostructures was found to considerably increase their photocatalytic activity. The observed increase in the RhB decomposition rate constant was 2.75 and 1.9 fold for the CdZnS/g-C_3N_4 and $ZnIn_2S_4$/g-C_3N_4 heterostructures, respectively. According to the band diagram, the synthesized heterostructures were found to exhibit the type-II and Z-scheme heterojunctions. Interactions of active particles with dye molecules were analyzed and it was found that oxidation of RhB occurs mainly through interactions with $O_2 \cdot^-$ species that form from oxygen molecules adsorbed on the surface of the catalyst.

Supplementary Materials: The following supporting information can be downloaded at: https://www.mdpi.com/article/10.3390/c9030085/s1, Table S1: Crystalline phases parameters.

Author Contributions: Conceptualization, R.R.S. and D.O.S.; methodology, R.R.S.; software, Z.M.M.; validation, R.R.S., Y.G.G. and A.T.G.; formal analysis, Z.M.M., A.F.S. and K.V.K.; investigation, R.R.S., K.V.K., A.F.S. and A.T.G.; resources, Y.G.G.; data curation, D.O.S.; writing—original draft preparation, R.R.S.; writing—review and editing, R.R.S. and Y.G.G.; visualization, D.O.S.; supervision, Y.G.G.; project administration, Y.G.G.; funding acquisition, A.T.G. and Y.G.G. All authors have read and agreed to the published version of the manuscript.

Funding: Photocatalytic studies were carried out (R. Shamilov, Yu. Galyametdinov) with the financial support of the Ministry of Science and Higher Education of the Russian Federation within the framework of the state order for the provision of public services (performance of work) dated 29 December 2022 No. 075-01508-23-00. Research topic "Creation of scientific foundations for obtaining

new multifunctional materials for a wide range of applications." Z. Muzipov and D. Sagdeev thank RSF Fund (No. 20-73-10091) for supporting synthesis and characterization of samples. A. Gubaidullin and A. Saifina acknowledge the financial support from the government assignment for FRC Kazan Scientific Center of RAS.

Data Availability Statement: The data presented in this study are available on request from the corresponding author.

Acknowledgments: The authors express their gratitude to the Center for Collective Use (CCU) of scientific equipment "Nanomaterials and Nanotechnologies" of the Kazan National Research Technological University with the financial support of the Ministry of Science and Higher Education of the Russian Federation under agreement № 075-15-2021-699. The authors gratefully acknowledge the Assigned Spectral-Analytical Center of FRC Kazan Scientific Center of RAS for the opportunity to fulfill the PXRD experiments. The authors are grateful to Sapegina A.O. for performing some of the diffraction studies.

Conflicts of Interest: The authors declare no conflict of interest.

References

1. Zhang, M.; Yang, Y.; An, X.; Hou, L.A. A critical review of g-C_3N_4-based photocatalytic membrane for water purification. *Chem. Eng. J.* **2017**, *391*, 72–123. [CrossRef]
2. Wei, Z.; Liu, J.; Shangguan, W. A review on photocatalysis in antibiotic wastewater: Pollutant degradation and hydrogen production. *Chin. J. Catal.* **2020**, *41*, 1440–1450. [CrossRef]
3. Thompson, W.A.; Sanchez Fernandez, E.; Maroto-Valer, M.M. Review and analysis of CO_2 photoreduction kinetics. *ACS Sustain. Chem. Eng.* **2020**, *8*, 4677–4692. [CrossRef]
4. Bora, L.V.; Mewada, R.K. Visible/solar light active photocatalysts for organic effluent treatment: Fundamentals, mechanisms and parametric review. *Renew. Sustain. Energy Rev.* **2017**, *76*, 1393–1421. [CrossRef]
5. Xu, F.; Mo, Z.; Yan, J.; Fu, J.; Song, Y.; El-Alami, W.; Wu, X.; Li, H.; Xu, H. Nitrogen-rich graphitic carbon nitride nanotubes for photocatalytic hydrogen evolution with simultaneous contaminant degradation. *J. Colloid Interface Sci.* **2020**, *560*, 555–564. [CrossRef]
6. Akhundi, A.; Zaker Moshfegh, A.; Habibi-Yangjeh, A.; Sillanpää, M. Simultaneous dual-functional photocatalysis by g-C_3N_4-based nanostructures. *ACS ES&T Eng.* **2022**, *2*, 564–585. [CrossRef]
7. Wen, J.; Xie, J.; Chen, X.; Li, X. A review on g-C_3N_4-based photocatalysts. *Appl. Surf. Sci.* **2017**, *391*, 72–123. [CrossRef]
8. Fu, J.; Yu, J.; Jiang, C.; Cheng, B. g-C_3N_4-Based heterostructured photocatalysts. *Adv. Energy Mater.* **2018**, *8*, 1701503. [CrossRef]
9. Balakrishnan, A.; Chinthala, M. Comprehensive review on advanced reusability of g-C_3N_4 based photocatalysts for the removal of organic pollutants. *Chemosphere* **2022**, *297*, 134190. [CrossRef]
10. Raza, W.; Ahmad, K. Visible light-driven photocatalysts for environmental applications based on graphitic carbon nitride. In *Handbook of Nanomaterials and Nanocomposites for Energy and Environmental Applications*; Kharissova, O., Martínez, L., Kharisov, B., Eds.; Springer: Cham, Switzerland, 2020; pp. 1–25. [CrossRef]
11. Wang, J.; Fan, Q.; Kou, L.; Chen, H.; Xing, X.; Duan, W.; Jiang, K. LED-driven sulfamethazine removal and bacterial disinfection by a novel photocatalytic textile impregnated with oxygen vacancy-rich BiO_{2-x}/g-C_3N_4 hybrid. *Chem. Eng. J.* **2023**, *474*, 145590. [CrossRef]
12. Ahmad, K.; Khan, M.Q.; Alsalme, A.; Kim, H. Sulfur-doped graphitic-carbon nitride (S@ g-C_3N_4) as bi-functional catalysts for hydrazine sensing and hydrogen production applications. *Synth. Met.* **2022**, *288*, 117100. [CrossRef]
13. Dai, C.; Feng, Z.; Hu, Q.; Qiu, J.; You, J.; Guo, R.; Zhang, H. Recent progress in modification and composite strategies of graphitic carbon nitride as catalysts for heterogeneous photo-Fenton reaction. *Mater. Sci. Semicond. Process.* **2023**, *167*, 107807. [CrossRef]
14. Zhang, M.; Yang, Y.; An, X.; Zhao, J.; Bao, Y.; Hou, L.A. Exfoliation method matters: The microstructure-dependent photoactivity of g-C_3N_4 nanosheets for water purification. *J. Hazard. Mater.* **2022**, *424*, 127424. [CrossRef]
15. Ma, L.; Fan, H.; Li, M.; Tian, H.; Fang, J.; Dong, G. A simple melamine-assisted exfoliation of polymeric graphitic carbon nitrides for highly efficient hydrogen production from water under visible light. *J. Mater. Chem. A* **2015**, *3*, 22404–22412. [CrossRef]
16. Cheng, L.; Xiang, Q.; Liao, Y.; Zhang, H. CdS-based photocatalysts. *Energy Environ. Sci.* **2018**, *11*, 1362–1391. [CrossRef]
17. Yu, K.; Zhang, T.; Wang, Y.; Wu, J.; Huang, H.; Yin, K.; Liao, F.; Liu, Y.; Kang, Z. Anchoring Co_3O_4 on CdZnS to accelerate hole migration for highly stable photocatalytic overall water splitting. *Appl. Catal.* **2023**, *324*, 122228. [CrossRef]
18. Yao, L.; Wei, D.; Ni, Y.; Yan, D.; Hu, C. Surface localization of CdZnS quantum dots onto 2D g-C_3N_4 ultrathin microribbons: Highly efficient visible light-induced H2-generation. *Nano Energy* **2016**, *26*, 248–256. [CrossRef]
19. Qin, D.; Xia, Y.; Li, Q.; Yang, C.; Qin, Y.; Lv, K. One-pot calcination synthesis of $Cd_{0.5}Zn_{0.5}S$/g-C_3N_4 photocatalyst with a step-scheme heterojunction structure. *J. Mater. Sci. Technol.* **2020**, *56*, 206–215. [CrossRef]
20. Feng, C.; Chen, Z.; Jing, J.; Sun, M.; Tian, J.; Lu, G.; Ma, L.; Li, X.; Hou, J. Significantly enhanced photocatalytic hydrogen production performance of g-C_3N_4/CNTs/CdZnS with carbon nanotubes as the electron mediators. *J. Mater. Sci. Technol.* **2021**, *80*, 75–83. [CrossRef]

21. Zhang, J.; Sun, J.; Maeda, K.; Domen, K.; Liu, P.; Antonietti, M.; Fu, X.; Wang, X. Sulfur-mediated synthesis of carbon nitride: Band-gap engineering and improved functions for photocatalysis. *Energy Environ. Sci.* **2011**, *4*, 675–678. [CrossRef]
22. Wang, J.; Sun, S.; Zhou, R.; Li, Y.; He, Z.; Ding, H.; Chen, D.; Ao, W. A review: Synthesis, modification and photocatalytic applications of $ZnIn_2S_4$. *J. Mater. Sci. Technol.* **2021**, *78*, 1–19. [CrossRef]
23. Yang, R.; Mei, L.; Fan, Y.; Zhang, Q.; Zhu, R.; Amal, R.; Yin, Z.; Zeng, Z. $ZnIn_2S_4$-Based photocatalysts for energy and environmental applications. *Small Methods* **2021**, *5*, 2100887. [CrossRef] [PubMed]
24. Chen, Z.; Guo, F.; Sun, H.; Shi, Y.; Shi, W. Well-designed three-dimensional hierarchical hollow tubular g-C_3N_4/$ZnIn_2S_4$ nanosheets heterostructure for achieving efficient visible-light photocatalytic hydrogen evolution. *J. Colloid Interface Sci.* **2022**, *607*, 1391–1401. [CrossRef] [PubMed]
25. Lin, B.; Li, H.; An, H.; Hao, W.; Wei, J.; Dai, Y.; Ma, C.; Yang, G. Preparation of 2D/2D g-C_3N_4 nanosheet@ $ZnIn_2S_4$ nanoleaf heterojunctions with well-designed high-speed charge transfer nanochannels towards high-efficiency photocatalytic hydrogen evolution. *Appl. Catal.* **2018**, *220*, 542–552. [CrossRef]
26. Hou, L.; Wu, Z.; Jin, C.; Li, W.; Wei, Q.; Chen, Y.; Wang, T. Flower-like dual-defective z-scheme heterojunction g-C_3N_4/$ZnIn_2S_4$ high-efficiency photocatalytic hydrogen evolution and degradation of mixed pollutants. *Nanomaterials* **2021**, *11*, 2483. [CrossRef]
27. *EVA v.11.0.0.3*; User Manual. SOCABIM: Île-de-France, France, 2005.
28. Bruker, A.X.S. *TOPAS V3: General profile and structure analysis software for powder diffraction data, Technical Reference*; Bruker AXS: Karlsruhe, Germany, 2005; 117p.
29. Zhang, R.; Ma, M.; Zhang, Q.; Dong, F.; Zhou, Y. Multifunctional g-C_3N_4/graphene oxide wrapped sponge monoliths as highly efficient adsorbent and photocatalyst. *Appl. Catal. B* **2018**, *235*, 17–25. [CrossRef]
30. Cao, S.; Low, J.; Yu, J.; Jaroniec, M. Polymeric photocatalysts based on graphitic carbon nitride. *Adv. Mater.* **2015**, *27*, 2150–2176. [CrossRef]
31. Jiang, L.; Lin, L.; Chen, D.; Wang, Y.; Li, M.; Shi, M.; Tang, Y.; Qiu, Y. Efficient visible-light photocatalytic MoS_2/C_3N_4 controllably constructed in the presence of surfactants. *Mater. Chem. Phys.* **2020**, *243*, 122643. [CrossRef]
32. Gataullin, A.R.; Bogdanova, S.A.; Galyametdinov, Y.G. Dispersion of fullerene C60 in organized media. *Liq. Cryst. Appl.* **2019**, *19*, 6–13. [CrossRef]
33. Gataullin, A.R.; Bogdanova, S.A.; Rakhmatullina, A.P.; Galyametdinov, Y.G. Dispersion of carbon nanotubes in solutions of oxyethylated isononylphenols. *Russ. J. Appl. Chem.* **2017**, *90*, 1795–1803. [CrossRef]
34. Chen, S.; Hu, Y.; Meng, S.; Fu, X. Study on the separation mechanisms of photogenerated electrons and holes for composite photocatalysts g-C_3N_4-WO_3. *Appl. Catal.* **2014**, *150*, 564–573. [CrossRef]
35. Gotipamul, P.P.; Dilly Rajan, K.; Khanna, S.; Rathinam, M.; Chidambaram, S. Bandgap engineering and plasmonically enhanced sun light photocatalyis in Au/$Cd_{1-x}Zn_xS$ nanocomposites. *J. Mater. Sci. Mater. Electron.* **2022**, *33*, 8385–8396. [CrossRef]
36. Rauf, M.A.; Ashraf, S.S. Fundamental principles and application of heterogeneous photocatalytic degradation of dyes in solution. *Chem. Eng. J.* **2009**, *151*, 10–18. [CrossRef]
37. Guo, R.T.; Wang, J.; Bi, Z.X.; Chen, X.; Hu, X.; Pan, W.G. Recent advances and perspectives of g-C_3N_4-based materials for photocatalytic dyes degradation. *Chemosphere* **2022**, *295*, 133834. [CrossRef] [PubMed]
38. Xia, Y.; Li, Q.; Lv, K.; Li, M. Heterojunction construction between TiO_2 hollowsphere and $ZnIn_2S_4$ flower for photocatalysis application. *Appl. Surf. Sci.* **2017**, *398*, 81–88. [CrossRef]